

See discussions, stats, and author profiles for this publication at: <https://www.researchgate.net/publication/256118112>

3-D Nanostructured Bilayer Solid Oxide Fuel Cell with 1.3 W/cm² at 450 °C.

ARTICLE *in* NANO LETTERS · AUGUST 2013

Impact Factor: 13.59 · DOI: 10.1021/nl402661p · Source: PubMed

CITATIONS

30

READS

141

5 AUTHORS, INCLUDING:



Jihwan an

Stanford University

30 PUBLICATIONS 231 CITATIONS

SEE PROFILE

Three-Dimensional Nanostructured Bilayer Solid Oxide Fuel Cell with 1.3 W/cm² at 450 °C

Jihwan An,[†] Young-Beom Kim,^{*,‡,§} Joonsuk Park,^{||} Turgut M. Gür,^{||} and Fritz B. Prinz^{†,||}

[†]Department of Mechanical Engineering, Stanford University, Stanford, California 94305, United States

[‡]Department of Mechanical Engineering, Hanyang University, Seoul 133-791, Korea

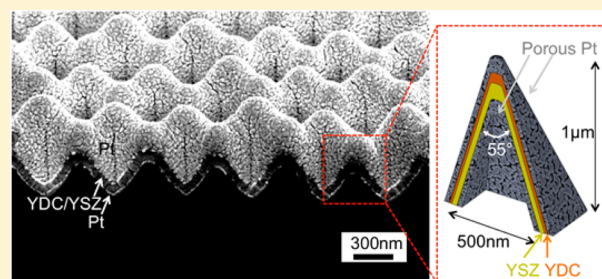
[§]Institute of Nano Science and Technology, Hanyang University, Seoul 133-791, Korea

^{||}Department of Materials Science and Engineering, Stanford University, Stanford, California 94305, United States

S Supporting Information

ABSTRACT: Obtaining high power density at low operating temperatures has been an ongoing challenge in solid oxide fuel cells (SOFC), which are efficient engines to generate electrical energy from fuels. Here we report successful demonstration of a thin-film three-dimensional (3-D) SOFC architecture achieving a peak power density of 1.3 W/cm² obtained at 450 °C. This is made possible by nanostructuring of the ultrathin (60 nm) electrolyte interposed with a nanogranular catalytic interlayer at the cathode/electrolyte interface. We attribute the superior cell performance to significant reduction in both the ohmic and the polarization losses due to the combined effects of employing an ultrathin film electrolyte, enhancement of effective area by 3-D architecture, and superior catalytic activity by the ceria-based interlayer at the cathode. These insights will help design high-efficiency SOFCs that operate at low temperatures with power densities that are of practical significance.

KEYWORDS: Solid oxide fuel cells, micro solid oxide fuel cells, low temperature solid oxide fuel cells, doped-ceria interlayer, atomic layer deposition, nanosphere lithography



Solid oxide fuel cells (SOFCs) offer many advantages including quiet operation under isothermal condition, high energy conversion efficiency with thermodynamic limits in excess of 80%, and diverse fuel flexibility by allowing the use of liquid and gaseous hydrocarbons as well as hydrogen.^{1–4} However, their high operating temperatures (usually >800 °C) pose stringent demands on materials selection to satisfy structural, chemical, and thermal stability and compatibility requirements, as well as costs for materials and fabrication.^{1,5,6} Attempts have been made to lower their operating temperature to intermediate ranges (600–800 °C)^{6–10} and even to lower (<500 °C) temperatures.^{11–17} Since both sintering and radiative heat transfer decrease at low temperatures, materials degradation mechanisms and insulation costs are significantly reduced.⁶ Low operating temperatures on the other hand significantly increase fuel cell losses and thus reduce cell performance and conversion efficiency.

The two main loss mechanisms for SOFCs are ohmic loss due to ionic transport through the electrolyte and activation loss (or polarization loss) from the slow cathode kinetics at the electrolyte/electrode interface. Ohmic loss can be minimized by using ultrathin (<100 nm) electrolytes,^{11–17} or by employing electrolytes with high ionic conductivity (e.g., La_{0.9}Sr_{0.1}Ga_{0.8}Mg_{0.2}O_{3–δ} (LSGM),¹⁸ Sm_{0.075}Nd_{0.075}Ce_{0.85}O_{2–δ} (SNDC)).¹⁹ However, these are in general chemically less

stable than the most commonly used yttria-stabilized zirconia (YSZ) electrolyte. Indeed, SOFCs with ultrathin YSZ electrolytes have reduced ohmic loss, but the cathode activation loss was still dominant, especially at low temperatures where oxygen reduction reaction (ORR) is quite sluggish with a high activation energy (~1 eV).²⁰

Our laboratory has successfully pursued several approaches toward reducing the activation loss. Catalytic interlayers such as doped CeO₂^{15,21,22} and doped Bi₂O₃⁶ enhanced the surface kinetics at the cathode interface and improved the power density. Similarly, grain-boundary engineering at the cathode interface also enhanced oxygen surface exchange.^{23–25} Moreover, structuring the membrane-electrode-assembly (MEA) in a three-dimensional (3-D) architecture also improved fuel cell performance significantly due to increased surface reaction area.^{13,14,16} Use of nanosphere lithography (NSL) and atomic layer deposition (ALD) made it possible to nanostructure 3-D MEAs.^{13,14}

The present study combines the three approaches above and reports the demonstration of 3-D nanostructured thin film low-temperature SOFC (LT-SOFC) with bilayer electrolyte that

Received: July 18, 2013

Revised: August 21, 2013

Published: August 26, 2013

delivers exceptionally high power density. By nanostructuring MEAs using NSL and ALD, we have doubled the effective surface reaction area. Also by interposing a nanogranular yttria-doped ceria (YDC) catalytic layer at the cathode interface, we have reduced activation loss by $\sim 35\%$. As a result, we were able to achieve peak power densities of 1.3 W/cm^2 at a considerably low temperature of 450°C . To our knowledge, this is the highest power density for LT-SOFCs reported to date below 500°C . We hope the three-prong fabrication strategy and the exciting cell performance result provide significant interest and opportunities for practical prospects of LT-SOFCs.

For the fabrication of the 3-D template structure, we employed a nanosphere lithography (NSL) technique as also has been used and published in our previous report.²¹ The SEM images of 3-D template (Figure S4), experimental details, and the schematic of the process flow (Figure S5) are provided in the Supporting Information. For the fabrication of the MEA, 50 nm thick YSZ electrolyte layer was grown on this 3-D nitride template at 250°C using ALD. On top of YSZ, YDC interlayer was grown at 500°C using PLD. Porous Pt layer was then deposited on top of YDC using DC sputtering as a cathode. After underlying nitride layer was removed using plasma etching, another porous Pt anode layer was deposited on the bottom face of the electrolyte. A detailed description of experimental conditions is available in the Supporting Information.

The performance of the fuel cells was measured at temperatures of 450, 400, and 360°C inside a homemade test chamber using a micromanipulating probe station developed earlier in our laboratory.¹³ Pure dry H_2 was supplied to the anode side as fuel while the cathode was exposed to ambient air. For fuel cell performance characterization, Gamry Potentiostats (Gamry Instruments) were used. Electrochemical impedance spectroscopy (EIS) measurements were performed at OCV as well as at a cell voltage of 0.5 V at 450, 400, and 360°C in the frequency range of 300 kHz to 1 Hz with the AC voltage signal amplitude of 100 mV. Actual temperatures of the chamber surface measured using IR thermometer (Fluke) were 440 ± 4 , 380 ± 3 , and $354 \pm 1^\circ\text{C}$ (for setting temperatures of 450, 400, and 360°C , respectively), which are slightly lower than the setting temperatures due to air cooling.¹⁴

Samples for TEM/STEM characterization were prepared by using a focused ion beam (FIB, FET Strata 235DB dual-beam FIB/SEM) lift-out technique. TEM/STEM images were recorded using a FEI Tecnai G2 F20 X-TWIN operated at 200 kV. X-ray energy dispersive spectroscopy (EDS) was performed with STEM probe of 0.2 nm in diameter and 0.25 nm step size. The recording time for each spot was 500 ms.

Figure 1a–d show the SEM images of the fabricated 3-D thin-film SOFC MEA. The window size—the projected area of the electrochemically active region—of the freestanding MEA is $43 \times 43 \mu\text{m}^2$ (Figure 1b) with the Si wafer opening to $585 \times 585 \mu\text{m}^2$ (Figure 1a) on the bottom side. Close-packed tetragonal pyramid structures were fabricated as shown in Figure 1c. The cross-sectional images of the free-standing MEA (Figure 1d) taken at 45° tilt show that the MEA consists of 60 nm-thick composite electrolyte with porous Pt electrodes on both sides. For the composite electrolyte, atomic layer deposition (ALD) was utilized for fabricating the YSZ film, while pulsed laser deposition (PLD) was used to coat the YDC film on the cathode side of YSZ. The dimensions of the pyramid structure are $\sim 500 \text{ nm}$ in base length and $\sim 1 \mu\text{m}$ in height as shown in Figure 1e. Based on the geometry shown in

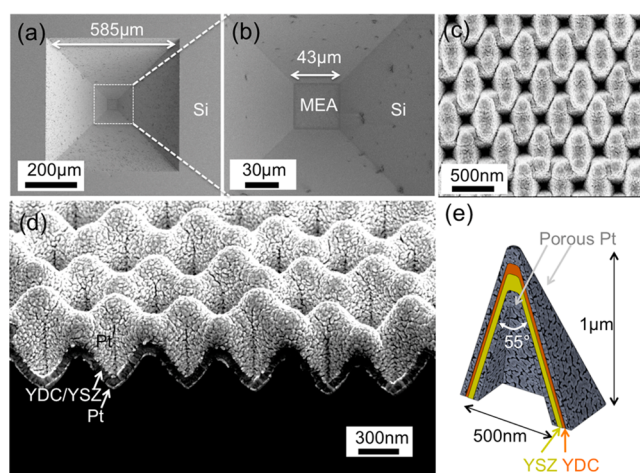


Figure 1. SEM images of the 3-D thin-film SOFC. (a) Anode side with Si support. (b) MEA ($43 \times 43 \mu\text{m}^2$) supported by Si backbone. (c) Top view (cathode side) of the MEA. (d) 45° tilted view of the cross-section of free-standing membrane (Pt/YDC/YSZ/Pt). (e) Schematic of the cross-section of a single pyramid structure.

SEM images, the ratio of the surface area to the projected area (i.e., area enhancement factor) is approximately 2.

To provide structural and compositional information with a finer resolution, transmission electron microscopy (TEM)/scanning TEM (STEM) analysis associated with diffraction and X-ray energy dispersive spectroscopy (EDS) were used. Bright-field TEM and STEM images of the MEA are shown in Figure 2a and b, respectively. YSZ and YDC layers in the composite electrolyte are clearly shown in the image by the difference in contrast, and their thicknesses are about 50 and 10 nm, respectively. Note that the thickness of the YDC layer on the slanted wall of the MEA (Figure 2a) is only a half of the thickness on the planar substrate (i.e., 20 nm). Similarly, the

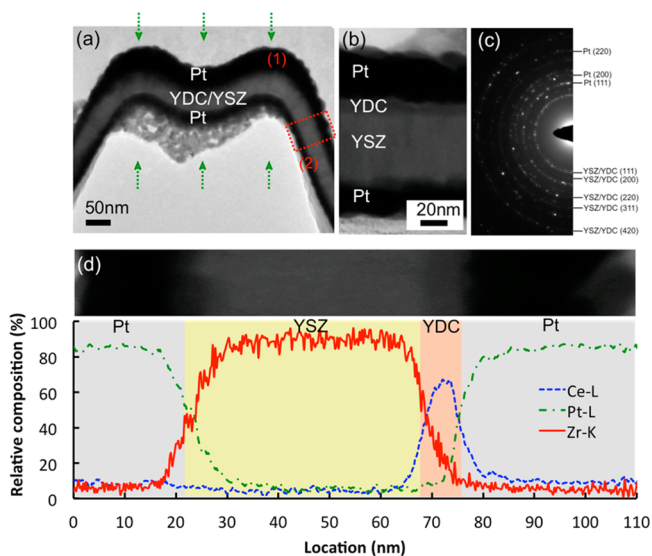


Figure 2. TEM/STEM images with diffraction and EDS. (a) Bright-field TEM image of the cross-section of the freestanding MEA. The green-dotted lines represent the direction of the Pt sputtering. (b) Zoomed-in STEM image of the red-dotted area (slanted wall) in a. (c) SAD pattern of the area shown in b. (d) STEM-EDS elemental line profiles across the MEA. The image of the analyzed area is on top of the profile.

thickness of Pt layer also varies from ~ 80 nm (thickest, point (1) in Figure 2a) at the region whose normal vector is parallel to the sputtering direction (green dotted line) down to ~ 30 nm (thinnest, point (2) in Figure 2a) at the slanted wall. These variations of the film thicknesses are to be expected due to the line-of-sight nature of the physical vapor deposition (PVD) methods (e.g., pulsed laser deposition (PLD), sputtering, etc.). However, despite the variations in thicknesses, the entire area of the template structure was coated with the YDC cathodic interlayer and porous Pt catalyst layer, which resulted in the successful operation of the 3-D fuel cell. This was possible because the slanted walls of the template permitted the use of inherently directional PVD methods for conformal coating of YDC and Pt layers.¹³ On the contrary, the thickness of the YSZ layer (~ 50 nm) is almost perfectly uniform over the whole area because of the superior conformality of the ALD process.^{14,16} Selective area diffraction (SAD) pattern (Figure 2c) of the area shown in Figure 2b reveals that YSZ/YDC/Pt films are nanocrystalline. Moreover, atomic force microscopy (AFM) image of the YDC surface (Figure S1) indicates that the surface of YDC layer is composed of nanoscale grains that are 38 ± 2 nm in diameter. The nanogranular surface structure is known to be beneficial in lowering the cathodic activation loss at the cathode/electrolyte interface due to enhanced oxygen surface exchange at the grain boundaries compared to that at the grain bulk.^{23–25} Also in the compositional analysis shown in Figure 2d, the STEM-EDS profile confirms that the 3-D layered MEA structure of Pt(cathode)/YDC(~ 10 nm)/YSZ(~ 50 nm)/Pt(anode) does not show any sign of intermixing that could lead to the formation of ionically blocking solid solution between the layers.²⁶

Contributions of individual losses to the total cell loss were determined by impedance analysis. The electrochemical impedance spectra (EIS) of the nanostructured bilayer MEA were taken at different cell voltages between 360 and 450 °C. Figure 3 shows the representative Nyquist plot obtained at 450

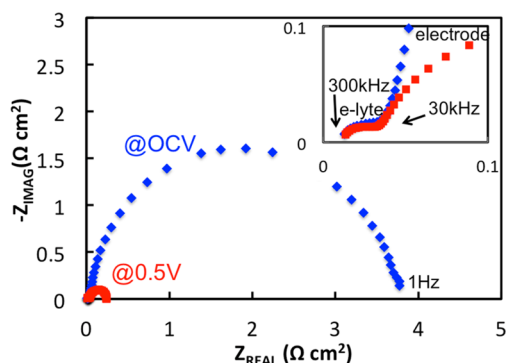


Figure 3. Nyquist plot of 3-D structured bilayer MEA at 450 °C at OCV (blue diamond dots) and at a cell voltage of 0.5 V (red square dots). The upper right inset shows the zoomed-in plot ($Z_{\text{REAL}} < 0.1 \Omega \text{ cm}^2$, $-Z_{\text{IMAG}} < 0.1 \Omega \text{ cm}^2$).

°C. Similarly, Nyquist plots at 400 and 360 °C are shown in Figure S2. The spectra consist of two semicircles; one at the high-frequency regime (300 kHz to 30 kHz) and the other at the low-frequency regime (30 kHz to 1 Hz). The high-frequency semicircle is independent of various cell voltage conditions, while the low-frequency semicircle is highly affected by the applied cell voltage. This suggests that the impedance value obtained from the high-frequency semicircle represents

the ohmic resistance due to ionic transport through the electrolyte membrane.²⁷ The low-frequency semicircle represents the polarization resistance mainly at the cathode, because the cathode polarization loss is known to be significantly larger than the anode polarization loss especially in the low-temperature regime.^{20,27} Since the ionic conductivity of YDC is more than 1 order of magnitude higher than that of YSZ in the measured temperature regime,¹ while its thickness is 1/5 the thickness of YSZ, one can safely assume that ohmic resistance of the composite electrolyte is dominated primarily by YSZ. The Arrhenius plot (Figure S3) shows that the activation energy (0.87 eV) is similar to that of the previously reported value (0.88 eV) for YSZ.¹ This supports our assumption for the overall resistance of the YDC/YSZ composite electrolyte. The calculated ionic conductivity of YSZ from the measured ohmic resistance is $1.5 \times 10^{-4} \text{ S/cm}$ at 450 °C. This value is slightly lower than the reference values,^{1,14} possibly due to interfacial resistance between YSZ and YDC layers. The second loop is significantly larger than the first loop, implying that the polarization loss is still dominant over the ohmic loss. It should be noted, however, that the size of the second loop at OCV in this work ($\sim 3.8 \Omega \text{ cm}^2$) is approximately 35% smaller than that in our group's previous report on a similarly nanostructured MEA with YSZ-only electrolyte ($\sim 6 \Omega \text{ cm}^2$).¹⁴ Considering that the contribution from cathodic polarization dominates the total cell loss at temperatures below 500 °C, we can postulate that the decrease in cathodic loss stems from the enhanced catalytic activity at the cathode/electrolyte interface provided by the YDC interlayer.

Figure 4 shows the voltage–current–power (V – I – P) behavior of the 3-D MEA at 450 °C, 400 °C, and 360 °C.

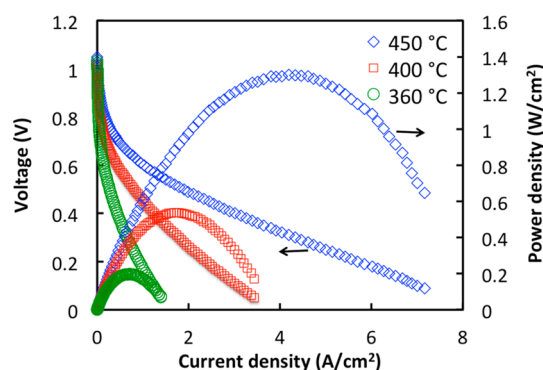


Figure 4. Cell voltage–current–power (V – I – P) curves at 450, 400, and 360 °C.

The open circuit voltages (OCVs) are in the range of 1.02–1.08 V. These values are close to thermodynamic limit (~ 1.1 V) at this temperature regime, which implies that the cathode and the anode are electronically and chemically isolated. The peak power densities obtained for the 3-D bilayer MEA at 450 °C, 400 °C, and 360 °C are 1.30 W/cm², 0.54 W/cm², and 0.20 W/cm², respectively. The performance of the MEA decreased by 30% after the first hour of operation possibly due to reduction in the triple phase boundary density and stabilized at that level for additional 2 h of operation (Figure S7).

The electrochemical characteristic of the 3-D MEA is further examined by Tafel analysis. Figure 5a shows the Tafel plot ($\ln(j)$ – η_{act} plot) obtained from the I – V curves shown in Figure 4. The exchange current densities (j_0) at 450, 400, and 360 °C

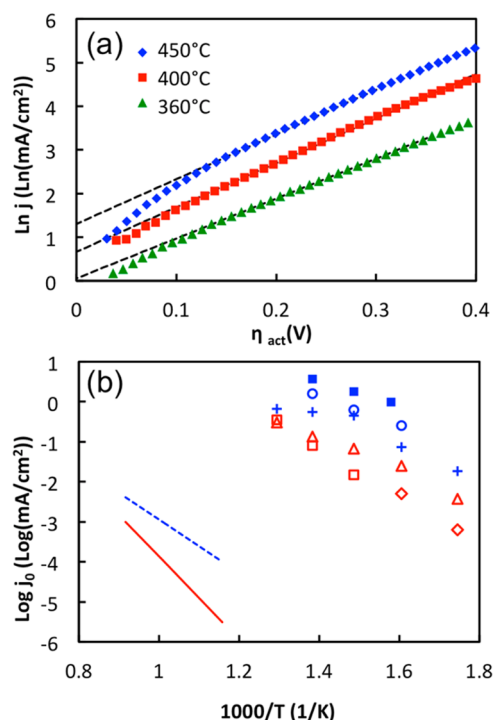


Figure 5. (a) Tafel (η_{act} vs $\ln(j)$) plot based on the current–voltage curves. (b) $1000/T$ vs exchange current density (j_0) plots for the nanocrystalline YDC/Pt interface (■: the present work (E_a : 0.58 eV), ○: from ref 24 (E_a : 0.62 eV), +: from ref 22 (E_a : 0.76 eV), shown in blue), the nanocrystalline YSZ/Pt interface (□: from ref 14 (E_a : ~1.4 eV, extracted from Figure 4 of ref 14), ◇: from ref 12 (E_a : ~1.1 eV, extracted from Figure 6 of ref 12), △: from ref 26 (E_a : 0.86 eV, shown in red), the single crystal YSZ/Pt (E_a : ~2.0 eV, extracted from Figure 7 of ref 29) (red solid line) and the sintered YDC/carbon (E_a : ~1.3 eV, extracted from Figure 7 of ref 29) (blue dotted line) are shown.

were 3.7, 1.8, and 1.0 mA/cm², respectively. Figure 5b presents the Arrhenius plot of $1000/T$ vs j_0 from the present work as well as from several other studies. The exchange current density of YDC shown in the present work is approximately 1 order of magnitude higher than that of YSZ at 450 °C. This agrees well with the previous papers reporting 1–2 orders of magnitude difference in oxygen surface exchange coefficient between YSZ and YDC at this temperature.^{28,29} Also note that the j_0 from the present work is 2–3 times larger than that from ref 24, both of which are for YDC/Pt interfaces. We speculate that this is because the average grain size of YDC at the surface of our sample (38 ± 2 nm, Figure S1) is smaller than that of the sample investigated in ref 24 (52 ± 15 nm). Previous investigations in our laboratory have shown that the YDC grain-boundary is catalytically more active than the grain-core for the oxygen reduction reaction,²⁴ which is known to be the

rate-determining step in LT-SOFC operation.²⁰ Moreover, it has been reported that the exchange current at the YDC/Pt interface shows a lower activation energy (E_a) than that at the YSZ/Pt interface due to the superior catalytic activity of the YDC compared to the YSZ.^{28,29} Indeed, the E_a obtained in this work (0.58 eV) is significantly lower than the E_a (~1 eV) reported on nano/microgranular YSZ/Pt interfaces.^{12,14,22} Also the E_a in the present work is close to the E_a (0.62–0.66 eV) our group reported for similarly nanogranular YDC surface²⁴ and to the E_a (0.6 eV) that Manning et al.³⁰ reported earlier for gadonia doped ceria (GDC) surface in this temperature regime (<700 °C). Compared to the E_a (~1.3 eV, extracted from Figure 3 in ref 28) for sintered YDC surface, the E_a in the present work is significantly lower, which also implies that the surface grain-boundary is catalytically active site for oxide-ion incorporation. We can therefore conclude that the enhanced electrode kinetics at the cathode shown in the present work is due to large j_0 and low E_a enabled jointly by both the superior catalytic activity of the YDC layer and the nanogranular structure of the electrolyte surface. The detailed description about how the Tafel plot was obtained and how the E_a was extracted is provided in the Supporting Information.

Table 1 compares the peak power densities achieved in the present work with others recently published on thin-film LT-SOFCs. The peak power density of our 3-D corrugated bilayer electrolyte cell is 2.2–2.5 times and 1.5–3.9 times larger than that of the planar YSZ electrolyte cell at 450 and 400 °C, respectively. As the thickness of the YSZ electrolyte in these studies are comparable, we attribute the observed enhancement to two separate contributions: one due to the catalytic interlayer (i.e., nanogranular YDC) and the other due to larger surface area. The peak power density of the bilayer cell of the present study is larger by a factor of 1.6 at 450 °C than the previously reported nanostructured cell with similar area enhancement but with YSZ-only electrolyte.¹⁴ We attribute this enhancement to the catalytic YDC bilayer, which helped reduce cathode polarization loss. This is also supported by EIS result showing a decreased polarization impedance loop as mentioned above. A similar power enhancement due to YDC was also observed when planar YSZ cell performance was compared with the planar YSZ+YDC cells.¹⁵ Furthermore, comparing the peak power density of our cell with that of the planar YSZ+YDC electrolyte cell without 3-D structuring indicates an enhancement of 1.8, which scales approximately with the area enhancement factor (~2). The slight discrepancy between the surface area and the power density enhancement seems to come from the nonuniform thicknesses of the YDC and the Pt layers due to the limitation of PVD methods (shown in Figure 2). Indeed, our group previously reported the decrease of power density of MEAs when the YDC interlayer is thinner than ~20 nm because below this thickness there is

Table 1. Peak Power Densities of Recently Reported LT-SOFCs at 400–450 °C

reference	structure	electrolyte material (thickness)	peak power density (W/cm ²)	
			450 °C	400 °C
11, 14–16	planar	YSZ (50–80 nm)	0.53–0.6	0.14–0.36
Huang et al. ¹¹	planar	YSZ (50 nm) + YDC(50 nm)	N/A	0.40
Su et al. ¹⁶	cup-shaped	YSZ (80 nm)	0.86	0.68
Fan et al. ¹⁵	planar	YSZ (70 nm) + YDC (10 nm)	0.71	0.46
Chao et al. ¹⁴	corrugated	YSZ (80 nm)	0.82	0.36
this work	corrugated	YSZ (50 nm) + YDC (10 nm)	1.30	0.54

insufficient coverage of the YDC layer over the entire surface of the YSZ electrolyte.²¹ Similarly, Jiang et al. showed that the thickness of sputtered Pt electrode should be ~80 nm to maximize the triple-phase-boundary (TPB) density and therefore achieve the highest power density.³¹ These issues can be resolved if conformal thin-film coating methods, such as ALD and electrodeposition, instead of PVD methods are used for fabricating these components. It is also possible that the silicon nitride support layer was not completely removed since the etching rate of the slanted wall is different from that of the planar area due to the directionality of plasma etching. Despite these minor issues, the performance of the 3-D structured bilayer fuel cell reported here presents by far the best performance in terms of the peak power density among all other LT-SOFCs reported at temperatures 450 °C and below.

Superior cell performance was achieved with a 3-D bilayer nanostructured SOFC architecture that produced 1.3 W/cm² peak power density at 450 °C. To our knowledge, this is the highest SOFC performance reported in the literature for temperatures below 500 °C. Structural, microscopic, and electrochemical characterization of the cells were reported. Exciting results of the present study encourages further research in this direction and paves the way for the successful development of high performance SOFCs operating at low temperatures. Further progress in such areas including catalytic cathodes in improving the rate of the oxygen reduction reaction, understanding thermal and mechanical behavior of cell components, improving fabrication process steps for better quality films, as well as better control of interfaces across the SOFC architecture will all help advance both understanding and engineering of superior LT-SOFCs for potential applications.

■ ASSOCIATED CONTENT

■ Supporting Information

Supplementary figures and detailed descriptions of the sample preparation and the data postprocessing. This material is available free of charge via the Internet at <http://pubs.acs.org>.

■ AUTHOR INFORMATION

Corresponding Author

*E-mail: ybkim@hanyang.ac.kr. Tel.: +82-2-2220-0544. Fax: +82-2-2220-2299.

Notes

The authors declare no competing financial interest.

■ ACKNOWLEDGMENTS

J.A. gratefully acknowledges the financial support from Kwanjeong Educational Foundation. Y.-B.K. is grateful to the National Research Foundation (NRF) of the Korean Ministry of Education, Science, and Technology (MEST) (Grant No. 2012R1A1A1014689 and 2012R1A6A1029029) for its financial support. J.A., T.M.G., and F.B.P. gratefully acknowledge partial support from the Center on Nanostructuring for Efficient Energy Conversion (CNEEC) at Stanford University, an Energy Frontier Research Center funded by the U.S. Department of Energy, Office of Science, Office of Basic Energy Sciences under Award Number DE-SC0001060. Work at Stanford University was supported by the U.S. Department of Energy (DOE), Office of Science, Office of Basic Energy Sciences (BES), Materials Sciences and Engineering Division under Award No. DE-SC0001060.

■ REFERENCES

- (1) Steele, B. C. H.; Heinzel, A. *Nature* **2001**, *414*, 345–352.
- (2) Yamamoto, O. *Electrochim. Acta* **2000**, *45*, 2423–2435.
- (3) Minh, N. Q. *Solid State Ionics* **2004**, *174*, 271–277.
- (4) Park, S.; Vohs, J. M.; Gorte, R. J. *Nature* **2000**, *404*, 265–267.
- (5) Brandon, N. P.; Skinner, S.; Steele, B. C. H. *Annu. Rev. Mater. Res.* **2003**, *33*, 183–213.
- (6) Wachsman, E. D.; Lee, K. T. *Science* **2011**, *334*, 935–939.
- (7) Chen, X.; Wu, N. J.; Smith, L.; Ignatiev, A. *Appl. Phys. Lett.* **2004**, *84*, 2700–2702.
- (8) Lu, Z.; Zhou, X.; Fisher, D.; Templeton, J.; Stevenson, J.; Wu, N.; Ignatiev, A. *Electrochem. Commun.* **2010**, *12*, 179–182.
- (9) Jiang, Y.; Virkar, A. V. *J. Electrochem. Soc.* **2003**, *150*, A942–A951.
- (10) De Souza, S.; Visco, S. J.; De Jonghe, L. C. *Solid State Ionics* **1997**, *98*, 57–61.
- (11) Huang, H.; Nakamura, M.; Su, P.; Fasching, R.; Saito, Y.; Prinz, F. B. *J. Electrochem. Soc.* **2007**, *154*, B20–B24.
- (12) Shim, J. H.; Chao, C. C.; Huang, H.; Prinz, F. B. *Chem. Mater.* **2007**, *19*, 3850–3854.
- (13) Kim, Y. B.; Jung, H. J.; Kang, S. K.; Gür, T. M.; Sinclair, R.; Prinz, F. B. *Electrochem. Commun.* **2011**, *13*, 403–406.
- (14) Chao, C. C.; Hsu, C. M.; Cui, Y.; Prinz, F. B. *ACS Nano* **2011**, *5*, 5692–5696.
- (15) Fan, Z.; An, J.; Iancu, A.; Prinz, F. B. *J. Power Sources* **2012**, *218*, 187–191.
- (16) Su, P. C.; Chao, C. C.; Shim, J. H.; Fasching, R.; Prinz, F. B. *Nano Lett.* **2008**, *8*, 2289–2292.
- (17) Tsuchiya, M.; Lai, B.-K.; Ramanathan, S. *Nat. Nanotechnol.* **2011**, *6*, 282–286.
- (18) Yan, J.; Matsumoto, H.; Enoki, M.; Ishihara, T. *Electrochem. Solid-State Lett.* **2005**, *8*, A389–A391.
- (19) Ahn, J. S.; Omar, S.; Yoon, H.; Nino, J. C.; Wachsman, E. D. *J. Power Sources* **2010**, *195*, 2131–2135.
- (20) Adler, S. B. *Chem. Rev.* **2004**, *104*, 4791–4843.
- (21) Kim, Y. B.; Holme, T. P.; Gür, T. M.; Prinz, F. B. *Adv. Funct. Mater.* **2011**, *21*, 4684–4690.
- (22) Fan, Z.; Prinz, F. B. *Nano Lett.* **2011**, *11*, 2202–2205.
- (23) Shim, J. H.; Park, J. S.; Holme, T.; Crabb, K.; Lee, W.; Kim, Y. B.; Tian, X.; Gür, T. M.; Prinz, F. B. *Acta Mater.* **2012**, *60*, 1–7.
- (24) Kim, Y. B.; Park, J. S.; Gür, T. M.; Prinz, F. B. *J. Power Sources* **2011**, *196*, 10550–10555.
- (25) Lee, W.; Jung, H. J.; Lee, M. H.; Kim, Y. B.; Park, J. S.; Sinclair, R.; Prinz, F. B. *Adv. Funct. Mater.* **2012**, *22*, 965–971.
- (26) Price, M.; Dong, J.; Gu, X.; Speakman, S. A.; Payzant, E. A.; Nenoff, T. M. *J. Am. Ceram. Soc.* **2005**, *88*, 1812–1818.
- (27) Holme, T. P.; Pornprasertsuk, R.; Prinz, F. B. *J. Electrochem. Soc.* **2010**, *157*, B64–B70.
- (28) Steele, B. C. H. *J. Power Sources* **1994**, *49*, 1–14.
- (29) Steele, B. C. H. *Solid State Ionics* **1995**, *75*, 157–165.
- (30) Manning, P. S.; Sirman, J. D.; Kilner, J. A. *Solid State Ionics* **1997**, *93*, 125–132.
- (31) Jiang, X.; Huang, H.; Prinz, F. B.; Bent, S. F. *Chem. Mater.* **2008**, *20*, 3897–3905.